Deep Atlantic Ocean carbon storage and the rise of 100,000-year glacial cycles

Deep Atlantic Ocean carbon storage and the rise of 100,000-year glacial cycles

J.R. Farmer[1,2,3,4]*, B. Hönisch[1,2], L.L. Haynes[1,2], D. Kroon[5], S. Jung[5], H.L. Ford[2,6], M.E. Raymo[1,2], M. Jaume-Seguí[2,7], D.B. Bell[5], S.L. Goldstein[1,2], L.D. Pena[7], M. Yehudai[1,2], and J. Kim[2]

[1]Department of Earth and Environmental Sciences, Columbia University, USA

[2]Lamont-Doherty Earth Observatory of Columbia University, USA

[3]now at Department of Geosciences, Princeton University, USA

[4]now at Max-Planck Institut für Chemie, Mainz, Germany

[5]School of GeoSciences, University of Edinburgh, UK

[6]School of Geography, Queen Mary University of London, UK

[7]Department of Earth and Ocean Dynamics, University of Barcelona, Spain

*Corresponding Author: jesse.farmer@princeton.edu

Text: 2,592 words
Methods: 2,942 words
Figures: Four (three two-column 180 mm, one one-column 88 mm)
Figure Legends: 563 words

Over the past three million years, Earth's climate oscillated between warmer interglacials with reduced terrestrial ice volume and cooler glacials with expanded polar ice sheets. These climate cycles, as reflected in benthic foraminiferal oxygen isotopes, transitioned from dominantly 41-kyr to 100-kyr periodicities during the mid-Pleistocene (1,250 to 700 ka). Because orbital forcing did not shift at this time, the ultimate cause of this mid-Pleistocene transition (MPT) remains enigmatic. Here we present foraminiferal trace element (B/Ca, Cd/Ca) and Nd isotope data that demonstrate a tight linkage between Atlantic Ocean meridional overturning circulation and deep-ocean carbon storage across the MPT. Specifically, between 950 and 900 ka, carbonate ion saturation decreased by 30 μmol/kg and phosphate concentration increased by 0.5 μmol/kg coincident with a 20% reduction of North Atlantic Deep Water contribution to the abyssal South Atlantic. These results demonstrate that the glacial deep Atlantic carbon inventory increased by approximately 50 gigatons during the transition to 100-kyr glacial cycles. We suggest that the coincidence of our observations with evidence for increased terrestrial ice volume reflects how weaker overturning circulation and Southern Ocean biogeochemical feedbacks facilitated deep ocean carbon storage, which lowered atmospheric pCO_2 and thereby enabled expanded terrestrial ice volume at the MPT.

Cyclic glaciations are the primary feature of Earth's climate since the late Pliocene and occur at periodicities linked to variations in solar insolation[1]. However, the dominant periodicity of glaciations transitioned from 41-kyr to 100-kyr during the mid-Pleistocene without concomitant changes in external insolation forcing[2-5]. It has been

42 suggested that the emergence of high-amplitude 100-kyr cycles in surface and deep ocean
43 climate records during the MPT[4,5,6] relates to internal climate amplifiers ("feedbacks")[3],
44 including changes in ice sheet dynamics[3,5,6-11], ocean circulation[12,13], and interactions of
45 these processes with Earth's carbon cycle[10-14]. Although temporal resolution is low,
46 atmospheric pCO_2 reconstructions across the MPT show that glacial pCO_2 decreased by
47 ~30 μatm sometime between 1,000 and 800 ka[11,15,16], consistent with more voluminous
48 glacial ice sheets[10,17]. The missing glacial pCO_2 was most likely sequestered in the deep
49 ocean[18] as suggested by benthic foraminiferal carbon isotope records ($\delta^{13}C_b$)[5,14,19].
50 However, evidence from $\delta^{13}C_b$ reflects a combination of ocean circulation, air-sea gas
51 exchange, and ocean carbon content, which complicates quantitative reconstructions of
52 any one parameter[13,14,19]. Because reliable quantitative records of ocean carbonate
53 chemistry are sparse, it is debated how the ocean sequestered additional CO_2 at the
54 MPT[11,13]. Stronger quantitative constraints on deep ocean dissolved inorganic carbon
55 (DIC) and its relation to meridional overturning circulation (MOC) are needed to evaluate
56 whether, and by which mechanisms, the ocean stored additional carbon at the MPT.

57 Here we test the hypothesis that the onset of 100-kyr glacial cycles during the
58 MPT was facilitated by enhanced deep ocean carbon storage accommodated by reduced
59 Atlantic MOC[12,13]. We present the first paired reconstructions of deep ocean DIC content
60 and MOC using foraminiferal trace element (B/Ca, Cd/Ca) and Nd isotope proxies,
61 recorded in sediments from Ocean Drilling Program Site 1267 from the Southeast
62 Atlantic Ocean (Fig. 1). In combination with previously published MOC and trace
63 element reconstructions, our results indicate coeval MOC reduction and increased deep
64 Atlantic DIC after 950 ka. We evaluate the contribution of our DIC estimates to

atmospheric pCO_2 based on ocean CO_2 sequestration mechanisms identified by modeling studies of the Last Glacial Maximum (LGM, ~20 ka), and hypothesise a sequence of climatic events that link changes in ocean circulation, carbon cycle and Earth's cryosphere with the emergence of 100-kyr glacial cycles during the MPT.

Carbonate chemistry, nutrients, and MOC across the MPT

Site 1267 is located at 4.4 km water depth in the Angola Basin north of Walvis Ridge[20], within dense Atlantic Ocean bottom waters (Fig. 1b). These waters comprise two general endmembers with characteristic chemical properties: North Atlantic Deep Water (NADW) feeds the basin from the north, and Antarctic Bottom Water (AABW) from the south. High oxygen, low-CO_2 and nutrient-poor NADW carries a low Nd isotope ratio (expressed as more negative ε_{Nd}, Methods), while low oxygen, high-CO_2 and nutrient-replete AABW carries a more positive ε_{Nd} signature from admixed Pacific waters (Fig. 1). Because Walvis Ridge blocks AABW inflow from the south, AABW enters the Angola Basin via the Romanche Fracture zone (0°N), thereby limiting the contribution of the generally deeper AABW to abyssal Angola Basin waters today (Fig. 1b). However, Site 1267 exhibits higher nutrient conditions (indicated by low $\delta^{13}C_b$ values) during Pleistocene glaciations[21,22], suggesting that this location tracks the balance of NADW and AABW contributions to the deep Atlantic across the MPT.

The B/Ca and Cd/Ca ratios of the epibenthic foraminifer *Cibicidoides wuellerstorfi* reflect the deep-sea carbonate ion saturation state[23] ($\Delta[CO_3^{2-}]$) and phosphate concentration[24] ($[PO_4^{3-}]$), respectively (Methods). Changes in $\Delta[CO_3^{2-}]$ and $[PO_4^{3-}]$ are linked to changes in DIC through ocean biogeochemistry, and we apply these

87 proxies from Site 1267 alongside published B/Ca and Cd/Ca records from North Atlantic
88 Site 607[13,25] to quantitatively constrain deep Atlantic DIC across the MPT. Additionally,
89 ε_{Nd} of planktic foraminiferal Fe-Mn oxide coatings at Site 1267 records the local
90 expression of changes in NADW and AABW contributions to the deep Atlantic Ocean
91 and complements a more southerly reconstruction of MOC strength across the MPT[12].

92 Site 1267 geochemical data show pronounced shifts in circulation and chemical
93 properties between Marine Isotopic Stages (MIS) 26 (970 ka) and 22 (880 ka) (Fig. 2).
94 ε_{Nd} suggests an ~20% reduction in NADW contribution to the South Atlantic between
95 MIS 26/25 and MIS 23/22 (Methods), in agreement with records from Sites 1088 and
96 1090 located ~10° to the south[12] (Supplementary Fig. 1). These combined ε_{Nd} records
97 indicate that the MOC perturbation between MIS 26 and 22 exceeds any previously
98 studied glacial transition before 950 ka. This MOC reduction corresponds with abrupt
99 increases in deep water corrosivity and nutrient content as indicated by an ~30 µmol/kg
100 $\Delta[CO_3^{2-}]$ decrease and an ~0.5 µmol/kg $[PO_4^{3-}]$ increase at Site 1267 (Fig. 2c, d). This
101 chemical transition persisted for at least 500 kyr. Whereas bottom water $\Delta[CO_3^{2-}]$ was
102 near or above saturation ($\Delta[CO_3^{2-}] = 0$) prior to 950 ka, $\Delta[CO_3^{2-}]$ values after 950 ka were
103 consistently negative in both glacials and interglacials, and they equaled modern $\Delta[CO_3^{2-}]$
104 of -2 µmol/kg during interglacials MIS 19, 17, and 13 (Fig. 2c). Similarly, reconstructed
105 $[PO_4^{3-}]$ was significantly higher after 950 ka than before, and approached modern $[PO_4^{3-}]$
106 of 1.6 µmol/kg during MIS 19, 17, and 13 (Fig. 2d).

107 The B/Ca and Cd/Ca patterns displayed by our Site 1267 records are similar in
108 trend but more pronounced than observations at Site 607 in the North Atlantic[13,25] (Fig.
109 2c, d). Site 607 $\Delta[CO_3^{2-}]$ is higher and $[PO_4^{3-}]$ lower than at Site 1267 for the length of

110 the records (Fig. 2), consistent with continuously better ventilation in the deep North
111 Atlantic compared to the abyssal Southeast Atlantic between 1,400 and 400 ka.

112 **Quantifying deep Atlantic DIC increase**

113 Synchronous but opposing $\Delta[CO_3^{2-}]$ and $[PO_4^{3-}]$ reconstructions across the MPT
114 (Fig. 2c-d) suggest the deep Atlantic acquired additional respired carbon after 950 ka.
115 Whereas $[PO_4^{3-}]$ proportionally increases with DIC through the stoichiometric ratio of
116 carbon to phosphorous in organic matter[26], the CO_2 released during respiration decreases
117 $[CO_3^{2-}]$, lowering $\Delta[CO_3^{2-}]$ (Supplementary Fig. 2). Using the C:P ratio of organic matter
118 exported to the deep ocean (117±14:1, ref. 26), and making simplifying assumptions
119 about changes in Cd inventory and seawater Cd:P ratios (Supplementary Information),
120 we quantify deep Atlantic DIC change associated with the MOC shift around 950 ka
121 (MIS 25) in glacial and interglacial climates (Methods). In addition, we also estimate
122 DIC change from $\Delta[CO_3^{2-}]$ by assuming constant local alkalinity (following ref. 27,
123 Methods).

124 At South Atlantic Site 1267, glacial DIC after 950 ka increased by 50±16
125 µmol/kg reconstructed from $\Delta[CO_3^{2-}]$, and 49±24 µmol/kg from $\Delta[PO_4^{3-}]$, compared to
126 glacials before 950 ka (Fig. 3a, b). At North Atlantic Site 607, glacial DIC similarly
127 increased by 50±30 µmol/kg reconstructed from $\Delta[CO_3^{2-}]$, and 20±18 µmol/kg from
128 $\Delta[PO_4^{3-}]$ (all uncertainties 1*s*). Reconstructed DIC also increased during interglacials
129 after 950 ka; at Site 1267 by 44±24 µmol/kg from $\Delta[CO_3^{2-}]$ and by 42±16 µmol/kg from
130 $\Delta[PO_4^{3-}]$; at Site 607 by 23±23 µmol/kg from $\Delta[CO_3^{2-}]$ and by 10±18 µmol/kg from
131 $\Delta[PO_4^{3-}]$ (Fig. 3). The averaged deep Atlantic glacial DIC increase after 950 ka (42±15

μmol/kg) agrees with the 42±22 μmol/kg DIC increase reconstructed from benthic foraminiferal B/Ca between MIS 5a and 4 prior to the LGM[27]. The generally larger DIC increases at Site 1267 (Fig. 3a, b) likely reflect the southerly and deeper position of Site 1267 relative to Site 607, which makes Site 1267 a more sensitive indicator of the relative contributions of northern and southern sourced deep waters. Nevertheless, these similar DIC estimates from two independent proxies at separate locations lend confidence for a persistent deep Atlantic DIC increase after 950 ka that encompassed both glacial and interglacial climates.

Increased DIC after 950 ka is likely the consequence of a more aged deep-water body in the deep Atlantic, with accumulated respired CO_2 and nutrients. Nd isotope ratios show that this aged deep water is associated with reduced NADW. Glacial ε_{Nd} values became more positive after 950 ka at Sites 1088, 1090 and 1267 (Fig. 3c, Supplementary Fig. 1), indicating reduced NADW and/or enhanced AABW. Interglacial ε_{Nd} values also show more positive values after 950 ka compared with before MIS 23 at Site 1267, indicating that reduced MOC after 950 ka was not limited to glacial climates (Methods). Covariance between ε_{Nd}, $\Delta[CO_3^{2-}]$ and $[PO_4^{3-}]$ at Site 1267 confirms that MOC and bottom water chemistry shifts are linked (Supplementary Fig. 3).

Implications for atmospheric pCO_2

As the Southern Ocean is the principal gateway for CO_2 to escape from the deep Atlantic into the atmosphere, changes in surface Southern Ocean properties that affect CO_2 leakage likely contribute to atmospheric CO_2 variations over Pleistocene glacial cycles[28,29]. These processes have also been invoked for the MPT[30], with recent studies

154 proposing that expanded Southern Ocean sea-ice extent[13] or increased iron availability[11]
155 lowered pCO_2 across the MPT. Upon comparing the temporal relationships of the
156 evidence, we propose that MPT pCO_2 reduction was closely related with reduced MOC
157 (Fig. 3). Whereas glacial Subantarctic iron deposition gradually increased between 1,400
158 and 1,100 ka[31] (Fig. 3f), ice core and proxy reconstructions suggest glacial pCO_2 did not
159 decrease before 1,000 ka[11,15,16] (Fig. 3d). Instead, glacial pCO_2 most likely decreased at
160 MIS 24-22, coeval with increased deep Atlantic DIC (Fig. 3a-b), lowered sea-level at
161 MIS 22[10,17] (Fig. 3g), and global surface ocean cooling[5,6]. This implies that reduced pCO_2
162 conforms to the more extensive glacial ice sheets of the 100-kyr world. Our prediction
163 that glacial pCO_2 was primarily reduced during MIS 24 and 22 agrees with pCO_2
164 simulations[32,33], and is testable with more detailed pCO_2 reconstructions from this critical
165 interval.

166 Lower pCO_2 is plausibly linked to increased deep Atlantic DIC by more complete
167 Southern Ocean nutrient utilisation and/or increased deep ocean stratification[29,34,35] after
168 950 ka. As indicated above, we do not believe that iron fertilisation primarily drove lower
169 pCO_2 after 950 ka. Instead, the coherent timing with MOC suggests a circulation-driven
170 process. The Southern Ocean's residual overturning circulation is driven by surface
171 density fluxes[36], and it has been proposed that changes to these density fluxes in glacial
172 climates are dynamically linked to deep ocean stratification[35,37] and pCO_2[38]. Specifically,
173 reduced rates of surface water densification combined with a northward shift of Southern
174 Ocean upwelling during glacial climates[38] increases the surface ocean residence time of
175 nutrient-rich waters, enhancing nutrient utilisation and CO_2 uptake before new AABW is
176 formed[38]. Both stratification and enhanced nutrient utilisation would increase deep ocean

177 DIC by preferentially segregating regenerated products (nutrients and carbon) in the deep
178 ocean. Deep ocean $\Delta[CO_3^{2-}]$ consequently decreases, driving a transient carbonate
179 ($CaCO_3$) dissolution event[39] that may increase alkalinity and foster additional ocean CO_2
180 storage[40,41], although the mechanisms and timescales of such alkalinity feedbacks are
181 debated[25]. Accounting for an alkalinity increase slightly elevates our estimate of deep
182 Atlantic DIC increase from B/Ca, but does not fundamentally change our results
183 (Methods).

184 The above conceptual arguments are supported by similar magnitudes of pCO_2
185 reduction at the MPT and in LGM model simulations of reduced MOC coupled to
186 reduced Southern Ocean CO_2 outgassing. Assuming our pooled estimate of glacial DIC
187 increase (42±15 μmol/kg) characterised the entire deep Atlantic below 3 km, then its
188 carbon inventory increased by 51±18 Gt C during glaciations after 950 ka (Methods).
189 Quantifying pCO_2 reduction from this DIC increase requires simulating the new
190 equilibrium reached between the ocean and atmospheric C reservoirs following the DIC
191 increase. Model simulations of the LGM provide a comparable constraint where the
192 effects of MOC and reduced Southern Ocean CO_2 outgassing on deep Atlantic DIC and
193 pCO_2 are quantified. In these simulations, combining reduced MOC with reduced
194 Southern Ocean CO_2 outgassing increases deep ocean DIC through a stronger biological
195 pump[27,29,43] and lowers pCO_2 by 13 to 45 ppm[29,42,43]. The consistency between these
196 pCO_2 estimates and the reconstructed 20-40 ppm glacial pCO_2 decrease across the
197 MPT[11,15,16] (Fig. 3e) supports a MOC and Southern Ocean pathway for MPT glacial
198 pCO_2 reduction. This implies that the 'ventilation volume' CO_2 sequestration hypothesis

199 for the LGM[29,43] first initiated with the major glacial MOC reduction after 950 ka[12], and
200 drove lower glacial pCO_2 levels during ensuing 100-kyr glacial cycles (Fig. 4).

201 Our averaged estimate for interglacial DIC increase (30±16 μmol/kg) implies a
202 deep Atlantic carbon inventory increase of 36±20 Gt C during interglacials after 950 ka.
203 This evidence for greater interglacial deep ocean carbon storage after 950 ka may have
204 contributed to the ~30 to 40 ppm lower pCO_2 during the "lukewarm" interglacials
205 between 450 and 900 ka[15,44], although identifying mechanisms for this requires further
206 study.

207 **Perspective**

208 An enduring mystery surrounding the MPT is how the cryosphere, ocean, and
209 carbon cycle interacted to initiate 100-kyr climate cycles at this particular time in Earth
210 history. While erosion of Northern Hemisphere regolith has been a central hypothesis for
211 the MPT[5,7,9,11], we suggest that an expanded Antarctic Ice Sheet played a key role in
212 unleashing the ocean carbon cycle feedbacks necessary for 100-kyr cycles (Fig. 4).
213 Atmospheric cooling associated with growth of the East Antarctic Ice Sheet to marine-
214 based margins around 1000 ka[8,45] (Fig. 3e) would have enhanced the production and
215 export of Antarctic sea-ice[37], expanding the spatial extent[35,37] but reducing the intensity
216 of surface water densification around Antarctica[38]. This increased residence time of
217 nutrient-rich waters would have enhanced nutrient utilisation and therefore CO_2 uptake.
218 Increased Antarctic surface "buoyancy loss" may also have directly facilitated expanded
219 AABW and enhanced deep ocean stratification[35,37], although we cannot rule out Northern
220 Hemisphere forcing of the MOC shift through reduced NADW production (Fig. 4c).

221 Future studies of Southern Ocean nutrient utilisation and deep ocean stratification across
222 the MPT can elucidate how these two mechanisms contributed to MPT pCO_2 decline.

223 In summary, our results demonstrate that the rise of 100-kyr ice age cycles is
224 intimately linked with increased deep ocean carbon storage associated with weakened
225 MOC. The key roles for ocean circulation and the carbon cycle in the natural climate
226 transition at the MPT raise critical questions on the future behaviour of these climate
227 components under anthropogenic warming. By the end of the century, Atlantic MOC is
228 projected to decrease by potentially similar magnitude (~20%) as the MOC reduction at
229 the MPT, albeit with high uncertainty[46,47]. While we have demonstrated that a weaker
230 MOC related to increased deep ocean carbon storage at the MPT, future deep ocean
231 carbon sequestration depends on how future MOC interacts with the evolution of the
232 biological pump and deep ocean stratification. In contrast to the MPT, projected future
233 reductions of Southern Ocean surface density[37,48] and reduced anthropogenic CO_2 uptake
234 by NADW under MOC weakening[49] may diminish the future carbon sequestration
235 potential of the deep Atlantic Ocean.

236

237 **References**

238 1. Hays, J.D., Imbrie J. & Shackleton, N. Variations in the Earth's Orbit: Pacemaker of
239 the Ice Ages. *Science* **194**, 1121-1132 (1976)

240 2. Pisias, N. & Moore, T. The evolution of Pleistocene climate: A time series approach.
241 *Earth Planet. Sci. Lett.* **52**, 450-458 (1981)

242 3. Imbrie, J. *et al*. On the structure and origin of major glaciation cycles 2. The 100,000-
243 year cycle. *Paleoceanography* **8**, 699-735 (1993).

244 4. Ruddiman, W.F., Raymo, M.E., Martinson, D.G., Clement, B.M. & Backman, J.
245 Pleistocene Evolution: Northern Hemisphere ice sheets and North Atlantic Ocean.
246 *Paleoceanography* **4**, 353-412 (1989).

247 5. Clark, P.U. *et al.* The middle Pleistocene transition: Characteristics, mechanisms, and
248 implications for long-term changes in atmospheric pCO_2. *Quat. Sci. Rev.* **25**,
249 3150-3184 (2006).

250 6. McClymont, E.L., Sosdian, S.M., Rossell-Melé, A. & Rosenthal, Y. Pleistocene sea-
251 surface temperature evolution: Early cooling, delayed glacial intensification, and
252 implications for the mid-Pleistocene climate transition. *Earth-Sci. Rev.* **123**, 173-
253 193 (2013).

254 7. Clark, P.U. & Pollard, D. Origin of the Middle Pleistocene Transition by ice sheet
255 erosion of regolith. *Paleoceanography* **13**, 1-9 (1998).

256 8. Raymo, M.E., Lisiecki, L.E. & Nisancioglu, K.H. Plio-Pleistocene Ice Volume,
257 Antarctic Climate, and the Global δ^{18}O Record. *Science* **313**, 492-495,
258 doi:10.1126/science.1123296 (2006).

259 9. Sosdian, S. & Rosenthal Y. Deep-Sea Temperature and Ice Volume Changes Across
260 the Pliocene-Pleistocene Climate Transitions. *Science* **325**, 306-310,
261 doi:10.1126/science1169938 (2009).

10. Elderfield, H. *et al.* Evolution of Ocean Temperature and Ice Volume Through the Mid-Pleistocene Climate Transition. *Science* **337**, 704-709 (2012).

11. Chalk, T.B., Hain, M.P. *et al.* Causes of ice age intensification across the Mid-Pleistocene Transition. *Proc. Natl. Acad. Sci.* **114**, 13114-13119, doi:10.1073/pnas.1702143114 (2017).

12. Pena, L.D. & Goldstein, S.L. Thermohaline circulation crisis and impacts during the mid-Pleistocene transition. *Science* **345**, 318-322, doi:10.1126/science.1249770 (2014).

13. Lear, C.H. *et al.* Breathing more deeply: Deep ocean carbon storage during the mid-Pleistocene climate transition. *Geology* **44**, 1035-1038, doi:10.1130/G38636.1 (2016).

14. Hodell, D.A., Venz, K.A., Charles, C.D. & Ninnemann, U.S. Pleistocene vertical carbon isotope and carbonate gradients in the South Atlantic sector of the Southern Ocean. *Geochem. Geophys. Geosyst.* **4**, 1004 (2003).

15. Hönisch, B., Hemming, N.G., Archer, A., Siddall, M. & McManus, J.F. Atmospheric carbon dioxide concentration across the mid-Pleistocene transition. *Science* **324**, 1551-1554 (2009).

16. Higgins, J.A. *et al.* Atmospheric composition 1 million years ago from blue ice in the Allan Hills, Antarctica. *Proc. Natl. Acad. Sci.* **112**, 6887-6891, doi:10.1073/pnas.1420232112 (2015).

17. Rohling, E.J., Foster, G.L., Grant, K.M., Marino, G., Roberts, A.P., Tamisiea, M.E. & Williams, F. Sea-level and deep-sea-temperature variability over the past 5.3 million years. *Nature* **508**, 477-482 (2014).

18. Broecker, W.S. Glacial to interglacial changes in ocean chemistry. *Prog. Oceanog.* **11**, 151-197 (1982).

19. Raymo, M.E., Oppo, D.W. & Curry, W. The mid-Pleistocene climate transition: A deep sea carbon isotopic perspective. *Paleoceanography* **12**, 546-559 (1997).

20. Zachos, J. *et al*. Site 1267. *Proc. ODP, Init. Repts.* **208**, 1-77 (2004).

21. Bell, D.B., Jung, S.J.A., Kroon, D., Lourens, L.J., & Hodell, D.A. Local and regional trends in Plio-Pleistocene $\delta^{18}O$ records from benthic foraminifera. *Geochem. Geophys. Geosyst.* **15**, 3304-3321 (2014).

22. Bell, D.B., Jung, S.J.A. & Kroon, D. The Plio-Pleistocene development of Atlantic deep-water circulation and its influence on climate trends. *Quat. Sci. Rev.* **123**, 265-282, doi: 10.1016/j.quascirev.2015.06.026 (2015).

23. Yu, J. & Elderfield, H. Benthic foraminiferal B/Ca ratios reflect deep water carbonate saturation state. *Earth Planet. Sci. Lett.* **258**, 73-86 (2007).

24. Boyle, E.A. Cadmium and $\delta^{13}C$ paleochemical distributions during the stage 2 Glacial Maximum. *Annu. Rev. Earth Planet. Sci.* **20**, 245-287 (1992).

25. Sosdian, S.M., Rosenthal, Y. & Toggweiler, J.R. Deep Atlantic Carbonate Ion and $CaCO_3$ Compensation During the Ice Ages. *Paeloceanography and Paleoclimatology* **33**, 546-562, doi:10.1029/2017PA003312 (2018).

26. Anderson, L.A. & Sarmiento, J.L. Redfield ratios of remineralization determined by nutrient data analysis. *Global Biogeochem. Cycles* **8**, 65-80 (1994).

27. Yu, J. *et al.* Sequestration of carbon in the deep Atlantic during the last glaciation. *Nature Geoscience* **9**, 319-324 (2016).

28. Sigman, D.M., Hain, M.P. & Haug, G.H. The polar ocean and glacial cycles in atmospheric CO_2 concentration. *Nature* **466**, 47-55, doi:10.1038/nature09149 (2010).

29. Hain, M.P., Sigman, D.M., & Haug, G.H. Carbon dioxide effects of Antarctic stratification, North Atlantic Intermediate Water formation, and Subantarctic nutrient drawdown during the last ice age: Diagnosis and synthesis in a geochemical box model. *Global Biogeochem. Cycles* **24**, GB4023 (2010).

30. Kemp, A.E.S, Grigorov, I., Pearce, R.B. & Naveira Garabato, A.C. Migration of the Antarctic Polar Front through the mid-Pleistocene transition: evidence and climatic implications. *Quat. Sci. Rev.* **29**, 1993-2009 (2010).

31. Martínez-Garcia, A. *et al*. Southern Ocean dust-climate coupling over the past four million years. *Nature* **476**, 312-315, doi:10.1038/nature10310 (2011).

32. Köhler, P. & Bintanja, R. The carbon cycle during the Mid Pleistocene Transition: The Southern Ocean Decoupling Hypothesis. *Clim. Past* **4**, 311-332, clim-past.net/4/311/2008 (2008).

33. Lisiecki, L.E. A benthic δ^{13}C-based proxy for atmospheric pCO_2 over the last 1.5 Myr. *Geophys. Res. Lett.* **37**, L21708, doi:10.1029/2010GL045109 (2010).

34. Adkins, J.F. The role of deep ocean circulation in setting glacial climates. *Paleoceanography* **28**, 1-23, doi:10.1002/palo.20046 (2013).

35. Ferrari, R. *et al.* Antarctic sea ice control on ocean circulation in present and glacial climates. *Proc. Natl. Acad. Sci.* **111**, 8753-8758, doi:10.1073/pnas.1323922111 (2014).

36. Marshall, J. & Speer, K. Closure of the meridional overturning circulation through Southern Ocean upwelling. *Nature Geoscience* **5**, 171-180, doi:10.1038/ngeo1391 (2012).

37. Jansen, M.F. Glacial ocean circulation and stratification explained by reduced atmospheric temperature. *Proc. Natl. Acad. Sci.* **114**, 45-50 (2017).

38. Watson, A.J., Vallis, G.K., & Nikurashin, M. Southern Ocean buoyancy forcing of ocean ventilation and glacial atmospheric CO_2. *Nature Geoscience* **8**, 861-864 (2015).

39. Broecker, W.S. & Peng, T.-H. The role of $CaCO_3$ compensation in the glacial to interglacial atmospheric CO_2 change. *Global Biogeochem. Cycles* **1**, 15-29 (1987).

339 40. Boyle, E.A. Vertical oceanic nutrient fractionation and glacial/interglacial CO_2 cycles.
340 *Nature* **331**, 55-56 (1988).

341 41. Archer, D. & Maier-Reimer, E. Effect of deep-sea sedimentary calcite preservation
342 on atmospheric CO_2 concentration. *Nature* **367**, 260-263 (1994).

343 42. Brovkin, V., Ganopolski, A., Archer, D. & Rahmstorf, S. Lowering of glacial
344 atmospheric CO_2 in response to changes in oceanic circulation and marine
345 biogeochemistry. *Paleoceanography* **22**, PA4204, doi:10.1029/2006PA001380
346 (2007).

347 43. Hain, M.P., Sigman, D.M. & Haug, The Biological Pump in the Past in *Treatise on*
348 *Geochemistry* 2nd edn, Vol. 8(18) (eds Mottl, M. J. & Elderfield, H.) 485–517
349 (2013).

350 44. Lüthi, D. *et al.* High-resolution carbon dioxide concentration record 650,000-800,000
351 years before present. *Nature* **453**, 379-382 (2008).

352 45. Billups, K., York, K. & Bradtmiller, L.I. Water Column Stratification in the Antarctic
353 Zone of the Southern Ocean During the Mid-Pleistocene Climate Transition.
354 *Paleoceanography and Paleoclimatology* **33**, doi:10.1029/2018PA003327 (2018).

355 46. Cheng, W., Chiang, J.C.H. & Zhang, D. Atlantic Meridional Overturning Circulation
356 (AMOC) in CMIP5 Models: RCP and Historical Simulations. *J. Clim.* **26**, 7187-
357 7197, doi:10.1175/jcli-d-12-00496.1 (2013).

358 47. IPCC. *Climate Change 2013: The Physical Science Basis. Contribution of Working*
359 *Group I to the Fifth Assessment Report of the Intergovernmental Panel on*

Climate Change [Stocker, T.F. *et al*. (eds.)]. Cambridge University Press, Cambridge, United Kingdom and New York, NY, USA. 1535 pp. doi:10.1017/CBO9781107415324 (2013).

48. Bernadello, R., Marinov, I., Palter, J.B., Sarmiento, J.L., Galbraith, E.D. & Slater, R.D. Response of the Ocean Natural Carbon Storage to Projected Twenty-First-Century Climate Change. *J. Clim.* **27**, 2033-2053, doi:10.1175/jcli-d-13-00343.1 (2014).

49. Pérez, F.F., Mercier, H., Vázquez-Rodríguez, M., Lherminier, P., Velo, A., Pardo, P.C., Rosón, G. & Ríos, A.F. Atlantic Ocean CO_2 uptake reduced by weakening of the meridional overturning circulation. *Nature Geoscience* **6**, 146-152, doi:10.1038/ngeo1680 (2013).

50. Schmieder, F., von Dobeneck, T. & Bliel, U. The Mid-Pleistocene climate transition as documented in the deep South Atlantic Ocean: Initiation, interim state and terminal event. *Earth Planet. Sci. Lett.* **179**, 539-549 (2000).

Acknowledgements. We thank Louise Bolge, Jennifer Falsetta, Katherine Esswein and Angela Dial for laboratory assistance, and Daniel Sigman for discussions. This research was supported by NSF OCE 14-36079. JRF acknowledges support from NSF DGE 16-44869. LP acknowledges support from the Ramón y Cajal program (MINECO, Spain).

Author Contributions. JF, LP, BH, MR, and SG designed the study; JF, DK, SJ and DB designed the sampling strategy; JF, LH and HF performed trace element analyses; MJ, MY and JK performed Nd sample processing and isotopic analyses; all authors contributed to interpretation of results and manuscript preparation.

Financial and non-financial competing interests. The authors declare no financial and non-financial competing interests.

Materials & Correspondence. Correspondence and materials requests should be directed to Jesse R. Farmer (jesse.farmer@princeton.edu).

Figure Captions.

Figure 1. Location of sediment cores and modern Atlantic Ocean hydrography. a) Site 1267[20] (cyan star) is located in the South Atlantic, along with cores comprising the SUSAS stack[50] (gray circles), and Sites 1088 and 1090[12,14,31]. Site 607[13,25] (orange diamond) is located in the North Atlantic. Colours denote surface ocean potential density from World Ocean Atlas 2013 data (www.nodc.noaa.gov/OC5/woa13/); white X's denote regions of modern-day deep-water formation. b) Meridional cross-section showing modern-day phosphate (colour) and salinity (contours indicate isolines) (composite of CLIVAR A20 and A13.5, www.clivar.org). Phosphate-poor NADW fills the Angola Basin to >4 km depth, while phosphate-rich AABW inflow is limited by Walvis Ridge. Phosphate-rich Antarctic Intermediate Water (AAIW) extends northward above 2 km depth. Plots created in Ocean Data View (http://odv.awi.de).

Figure 2. Site 1267 and 607 circulation and trace element records across the MPT. a) Site 1267 $\delta^{18}O_b$[21] (black) and $\delta^{13}C_b$[21,22] (brown); red and blue numbers denote interglacial and glacial stages, respectively. b) Site 1267 ε_{Nd}; opposite axis gives corresponding percentage North Atlantic sourced water (NAW, calculation in Methods). c) B/Ca from 607[13,25] (gray circles) and 1267 (filled squares); opposite axis gives $\Delta[CO_3^{2-}]$ (Methods). d) Cd/Ca from 607[13] (gray circles) and 1267 (outlined squares); opposite axis gives $[PO_4^{3-}]$ (Methods). Error bars are replicate 1*s*, and are greater than long-term internal precision (Methods). Red, blue and gray squares indicate Site 1267 interglacial, glacial and transitional samples, respectively. Horizontal lines in c) and d)

indicate modern $\Delta[CO_3^{2-}]$ and $[PO_4^{3-}]$ at 1267 (blue) and 607 (orange). Vertical gray shading highlights MIS 25 through 22.

Figure 3. Changes in ocean CO_2 feedbacks and climate across the MPT. ΔDIC reconstructed from $\Delta[CO_3^{2-}]$ (a) and $\Delta[PO_4^{3-}]$ (b) at Sites 1267 (filled squares) and 607 (open squares). c) South Atlantic MOC from ε_{Nd} at Sites 1267 (squares) and 1088[12] (circles). Red/blue symbols in a-c indicate interglacials/glacials, respectively. d) pCO_2 from EPICA Dome C[44] (black line), Allan Hills[16] (black bar at 1,000 ka), planktic foraminiferal boron isotopes (red/blue/gray circles are interglacials/glacials/transitional from ref. 15; cyan curve, ref. 11), and modeled[33]. Yellow shading indicates average pCO_2 for 0-420, 420-900, and 950-2,000 ka. e) Terrigenous mass accumulation rate from Site 745 indicating East Antarctic Ice Sheet activity[45]. f) Iron mass accumulation rate in the Subantarctic Atlantic (Site 1090)[31]. g) Eustatic sea level from South Pacific $\delta^{18}O_{sw}$[10] (cyan line) and Mediterranean planktic foraminifer $\delta^{18}O$[17] (yellow points).

Figure 4. Schematics of proposed coupling between cryosphere, Atlantic MOC, and carbon cycle responses across the MPT. Glacial Atlantic MOC cross-sections before and after 950 ka are in a) and c), respectively. b) and d) show Antarctic processes within dashed regions of a) and c). Curved arrows trace AABW and NADW pathways; arrow colour indicates $[PO_4^{3-}]$ (Fig. 1) and thickness indicates deep-water contribution (thicker is greater contribution). RFZ= Romanche Fracture Zone. Red arrows indicate ocean CO_2 release; orange dots indicate dust deposition. Black curved lines in b) and d) indicate brine rejection. EAIS= East Antarctic Ice Sheet. Before 950 ka, a smaller EAIS limits Antarctic sea-ice coverage, shortening the path for Antarctic surface waters before subduction, giving a larger fraction of unutilised nutrients in AABW and greater CO_2 release (b). NADW dominates Atlantic MOC (a). After 950 ka, EAIS expands to marine-based margins and sea-ice expands. Antarctic surface waters upwell farther north, travelling further before subduction, decreasing $[PO_4^{3-}]$ in AABW and lowering CO_2 outgassing (d). AABW dominates deep Atlantic circulation, effectively trapping CO_2 (cross-hatching, c).

430

Methods

ODP Site 1267 and sample selection. ODP Site 1267 (28°5.89' S, 1°42.66'E, 4.36 km water depth) was cored near the northwestern margin of Walvis Ridge in the Angola Basin[20]. Site 1267 chronology was established by aligning *Cibicidoides wuellerstorfi* $\delta^{18}O$[21] to the LR04 global $\delta^{18}O_b$ stack[51]. For this study, *C. wuellerstorfi* specimens >250 μm were picked from samples reflecting glacial-interglacial extremes (indicated by $\delta^{18}O_b$) spanning MIS 46 to MIS 12, and every 25 cm (every ~3 kyr) between MIS 30 and MIS 22 (Supplementary Fig. 4). Our records do not extend beyond MIS 12 due to limited *C. wuellerstorfi* in younger sediments. Glacial and interglacial extremes in B/Ca and Cd/Ca records from Site 607[13,25] were also selected based on $\delta^{18}O_b$ (Supplementary Fig. 4).

Trace element analyses. For Site 1267, six to twelve *C. wuellerstorfi* specimens were crushed between two methanol-cleaned glass slides and transferred to HCl-cleaned 0.5 mL polypropylene vials. When necessary, adjacent samples were combined to provide 200 to 300 μg of calcite. Crushed samples were cleaned via clay removal in methanol and boron-free MilliQ water, removal of Fe-Mn oxides and authigenic Mn carbonates by reduction with an ammonium-citric acid-buffered hydrazine ($NH_4(OH)$-$C_6H_8O_7$-N_2H_4) solution, organic oxidation with NaOH-buffered H_2O_2, and a weak acid leach with 0.001 N HNO_3 to remove any adsorbed contaminants, following standard protocols[52-54]. Samples were transferred to HCl-cleaned 2 mL polypropylene vials after the oxidation step. Initial tests showed elevated Mn and Fe concentrations (> 100 μmol/mol) without reductive cleaning, and thus reductive cleaning was performed on all samples. Removal of Fe and Mn phases is critical for reducing Cd blank[53] and does not affect B/Ca ratios[55]. All sample preparation was performed in a boron-free HEPA laminar flow bench at the Lamont-Doherty Earth Observatory (LDEO).

Cleaned samples were dissolved in 0.8 to 1.6 mL of ultrapure 2% HNO_3 immediately prior to analysis, with the volume of acid adjusted by sample mass to obtain ~50 ppm [Ca^{2+}] solutions. Trace element intensities were measured using a Thermo Scientific iCAP Q inductively coupled plasma mass spectrometer at LDEO[56] following methods adapted from ref. 57. Low mass element ^{11}B was measured in standard mode;

461 ^{23}Na, ^{27}Al, ^{43}Ca, ^{55}Mn, ^{56}Fe, and ^{111}Cd were measured in kinetic energy discrimination
462 mode using a He collision cell to minimise polyatomic interferences. To minimise matrix
463 effects, element intensities were corrected with an internal multi-element quality control
464 standard measured every ten samples. Concentrations and element ratios (relative to Ca)
465 were calculated from element intensities measured on a multi-element stock solution
466 prepared gravimetrically from trace element-grade stock solutions. This solution was
467 diluted to [Ca^{2+}] of 5 to 125 ppm and each dilution was then measured, creating
468 calibrations of element intensity to concentration. External precision was evaluated using
469 nine full procedural replicates from Site 1267, with 1*s* pooled replicate precision of ±6.6
470 μmol/mol for B/Ca and ±0.009 μmol/mol for Cd/Ca. Long-term internal precision (1*s*) of
471 an in-house quality control standard was ±2.9 μmol/mol for B/Ca and ±0.006 μmol/mol
472 for Cd/Ca.

473 Site 607 B/Ca and Cd/Ca ratios were previously measured via similar
474 protocols[13,25]. Pooled replicate precision (1*s*) for Site 607 B/Ca and Cd/Ca was ±5.9 and
475 ±0.007 μmol/mol, respectively[13]. No attempt was made to correct for laboratory B/Ca or
476 Cd/Ca offsets. If laboratory offsets existed, they would not change the results of our study
477 because each core was measured in separate laboratories and we independently calculate
478 ΔDIC from B/Ca and Cd/Ca variations within each core (see below).

479 **Neodymium isotope analyses.** Nd isotopes ($^{143}Nd/^{144}Nd$) were measured on Fe-Mn
480 encrusted planktic foraminifera[12,58]. Between 20 and 30 mg of planktic foraminifera from
481 the >300 μm size fraction were crushed, ultrasonicated and resuspended in MilliQ water
482 and methanol to remove detrital contaminants. Each sample was treated individually to
483 ensure that sufficient rinsing steps were applied. Cleaned fragments were dissolved in
484 dilute acetic acid, and the resulting solution centrifuged. The supernatant was transferred
485 to clean PFA beakers and Nd was separated using Eichrom Tru-Spec and Ln-Spec resins.
486 Nd isotopes were determined by multi-collector inductively coupled mass spectrometry
487 on a ThermoScientific Neptune-Plus at LDEO. Instrumental drift was corrected by
488 sample-standard bracketing (SSB) using JNdi-1 as the primary standard[59], with matching
489 standard and sample Nd concentrations. Nd isotopes are expressed as ε_{Nd} values, which
490 give deviations in parts per 10^4 from the average $^{143}Nd/^{144}Nd$ value of chondritic

meteorites (0.512638)[60]. External analytical reproducibility (±2*s*) was 0.28 and 0.43 εNd units (±0.000014 and 0.000021 absolute) for the two analytical sessions where Site 1267 samples were measured.

Converting B/Ca, Cd/Ca to DIC$_{resp}$. Global coretop calibration shows that *C. wuellerstorfi* B/Ca records $\Delta[CO_3^{2-}]$[23,61-63], where $\Delta[CO_3^{2-}] = [CO_3^{2-}]_{in\ situ} - [CO_3^{2-}]_{saturation}$. Site 607 and 1267 B/Ca was converted to $\Delta[CO_3^{2-}]$ using B/Ca (μmol/mol) = 1.14±0.04* $\Delta[CO_3^{2-}]$ (μmol/kg) + 176.6±1.0 (ref. 63).

Both $[CO_3^{2-}]_{in\ situ}$ and $[CO_3^{2-}]_{saturation}$ are relatively insensitive to changes in temperature, salinity, and pressure. For instance, projected changes in deep ocean temperature, salinity and pressure on glacial-interglacial timescales negligibly influence $\Delta[CO_3^{2-}]$ compared to instrumental B/Ca precision[64]. Therefore, downcore changes in $\Delta[CO_3^{2-}]$ primarily reflect changes in deep ocean $[CO_3^{2-}]_{in\ situ}$ driven by changes in the difference between total alkalinity (TA) and dissolved inorganic carbon (DIC) (Supplementary Fig. 2; ref. 27). If the quantity TA-DIC increases, the greater excess of TA relative to DIC implies a shift in DIC speciation toward CO_3^{2-} and thus increased $[CO_3^{2-}]$. Conversely, a decrease in the quantity TA-DIC implies DIC speciation shifts toward CO_2, and thus $[CO_3^{2-}]$ decreases.

Changes in $\Delta[CO_3^{2-}]$ at Sites 1267 and 607 are a function of TA and DIC (Supplementary Fig. 2):

$$\left(\Delta[CO_3^{2-}]_{measured} - \Delta[CO_3^{2-}]_{reference}\right) = 0.54 * (\Delta TA - \Delta DIC) \quad (1)$$

where $\Delta[CO_3^{2-}]_{measured}$—$\Delta[CO_3^{2-}]_{reference}$ gives the $\Delta[CO_3^{2-}]$ difference from a reference $\Delta[CO_3^{2-}]$ value (here, the average pre-950 ka interglacial $\Delta[CO_3^{2-}]$ of +14.8 μmol/kg at Site 1267 and +39.7 μmol/kg at Site 607), and ΔTA and ΔDIC are the differences in TA and DIC between each sample relative to average pre-950 ka interglacial TA and DIC. Note that while we use $\Delta[CO_3^{2-}]$ instead of $[CO_3^{2-}]_{in\ situ}$ (as used by ref. 27 and 52), Equation 1 is identical using either parameter because $[CO_3^{2-}]_{saturation}$ is assumed constant due to the small influence of temperature, salinity, and pressure variations on $[CO_3^{2-}]_{saturation}$ (see above). The slope of Equation 1 (k=0.54) is less than one due to a larger

519 contribution from non-carbonate species (particularly borate anion) to TA as the quantity
520 TA-DIC increases. We calculated *k* by varying TA and DIC at the present-day bottom-
521 water temperature (2.4°C), salinity (34.89) and pressure (4429 dbar) of Site 1267 in
522 CO2SYS (ref. 65). Following this for Site 607 also returns *k* of 0.54. In contrast, Yu *et*
523 *al.*[27] used *k*=0.59 from regression of oceanographic data below 2.5 km depth in the
524 Atlantic Ocean, but this approach includes influences from pressure, temperature, and
525 salinity variations within the dataset used for their regression. Our slope is more
526 appropriate because the expected temperature, salinity and pressure variations at Sites
527 1267 and 607 across the late Pleistocene are smaller than the present-day ranges of these
528 parameters in the Atlantic Ocean below 2.5 km depth.

529 Two processes primarily control deep ocean TA and DIC: organic matter
530 respiration and calcium carbonate ($CaCO_3$) dissolution (Supplementary Fig. 2). Explicitly
531 accounting for the effects of respiration and dissolution in Eq. 1 and substituting pre-950
532 ka interglacial $\Delta[CO_3^{2-}]$ for $\Delta[CO_3^{2-}]_{reference}$ gives:

533 $$\left(\Delta[CO_3^{2-}]_{measured} - 14.8\right) = 0.54 * \left((\Delta TA - \Delta DIC)_{resp} + (\Delta TA - \Delta DIC)_{diss}\right) \qquad (2)$$

534 for Site 1267. (For Site 607, 39.7 μmol/kg is subtracted from $\Delta[CO_3^{2-}]_{measured}$ to
535 normalize to average pre-950 ka interglacial $\Delta[CO_3^{2-}]$). Here *resp* and *diss* denote
536 changes from organic matter respiration and dissolution, respectively. Respiring 1 μmol
537 of organic matter in 1 kg seawater increases DIC by 1 μmol/kg and decreases TA by 0.14
538 μmol/kg (ref. 26). This decreases the quantity TA-DIC by 1.14 μmol/kg and thus
539 decreases $[CO_3^{2-}]_{in\ situ}$ by 0.62 μmol/kg. Dissolution of 1 μmol of $CaCO_3$ in 1 kg seawater
540 increases DIC by 1 μmol/kg and increases TA by 2 μmol/kg, which increases TA-DIC by
541 1 μmol/kg and thus raises $[CO_3^{2-}]_{in\ situ}$ by 0.54 μmol/kg. Using these stoichiometric ratios
542 of TA- and DIC-change during respiration and dissolution, Eq. 2 becomes:

543 $$\left(\Delta[CO_3^{2-}]_{measured} - 14.8\right)(\mu mol/kg) = 0.54 * \left(0.5\Delta TA_{diss} - 1.14\Delta DIC_{resp}\right) \qquad (3)$$

544 for Site 1267. As in Eq. 1, ΔTA_{diss} and ΔTA_{resp} values are calculated relative to pre-950
545 ka interglacial averages.

Equation 3 has three unknowns: $\Delta[CO_3^{2-}]$, ΔTA_{diss}, and ΔDIC_{resp}. B/Ca constrains $\Delta[CO_3^{2-}]$, but one more constraint is required to solve Eq. 3. One approach is to assume constant deep ocean alkalinity[27] (ΔTA_{diss}=0), which allows Eq. 3 to be solved for ΔDIC_{resp}. Previous applications of B/Ca to reconstruct DIC assumed constant TA over short study intervals[27,66] (<50 kyr). In contrast, our 1-Myr record covers a climate transition associated with notable changes in deep-sea carbonate sedimentation[25,49,67] (Supplementary Fig. 5). Thus, it may not be practical to assume that ΔTA_{diss}=0 (see below).

Lacking established paleo-proxies for TA, here we also calculate ΔDIC_{resp} using *C. wuellerstorfi* Cd/Ca, an independent nutrient proxy that is unlikely affected by ΔTA_{diss}. *Cibicidoides wuellerstorfi* Cd/Ca relates to deep ocean [Cd] through the following relationship:

$$[Cd]_{sw}(nmol/kg) = \frac{10*(Cd/Ca)_{C.wuellerstorfi}}{2.9} \quad (4)$$

where 2.9 is the partition coefficient of Cd into calcitic foraminifera below 3 km depth and 10 is the seawater $[Ca^{2+}]$ in mmol/kg[24,68,69]. $[Cd]_{sw}$ relates to $[DIC]_{resp}$ through stoichiometric relationships in seawater and organic matter. In the modern Atlantic Ocean, $[Cd]_{sw}$ is strongly, but nonlinearly, correlated with phosphate concentration ($[PO_4^{3-}]$)[70-73]. This nonlinearity might reflect Cd uptake by phytoplankton[71] possibly modulated by the local abundance of other trace elements[72]. Recent high-quality $[Cd]_{sw}$ measurements taken during the GEOTRACES program in the Atlantic Ocean[72-75] exhibit a strong nonlinear correlation to $[PO_4^{3-}]$, which is linearized by using the square root of $[Cd]_{sw}$ (Supplementary Fig. 2c):

$$[PO_4^{3-}](\mu mol/kg) = \frac{\sqrt{[Cd]_{sw}} - 0.062}{0.361} \quad (5)$$

Cibicidoides wuellerstorfi Cd/Ca is used to calculate $\Delta[Cd]_{sw}$ using Equation 4, and then ΔDIC_{resp} associated with $\Delta[Cd]_{sw}$ is calculated assuming a Redfield C:P ratio of 117±14:1 (ref. 26):

$$\Delta DIC_{resp}(\mu mol/kg) = (117 \pm 14) * \frac{\sqrt{\Delta[Cd]_{sw}} - 0.062}{0.361} \quad (6)$$

As in Equation 3, ΔDIC_{resp} and $\Delta[Cd]_{sw}$ are calculated as differences relative to pre-950 ka interglacial averages.

Reconstructed ΔDIC_{resp} from Cd/Ca (Equation 6) largely agrees with ΔDIC_{resp} calculated from B/Ca (Equation 3) assuming ΔTA_{diss}=0 over our study interval at Site 1267 (Supplementary Fig. 6). This correspondence argues against major variations in uncertainty sources that affect one—but not both—proxies. Specifically, this correspondence suggests that any changes in ΔTA_{diss} (influencing B/Ca) are smaller than the (relatively large) uncertainty on B/Ca-derived ΔDIC_{resp} (discussed below). Similarly, this argues against secondary influences on Cd/Ca-derived ΔDIC_{resp} estimates (Supplementary Information).

Quantifying deep Atlantic carbon storage. Following ref. 27, we quantify deep Atlantic carbon storage as follows:

$$\Delta C(Gt) = \frac{-12.011 * \Delta DIC_{Atlantic>3km} * m_{Atlantic>3km}}{10^{21}} \quad (7)$$

where $\Delta DIC_{Atlantic>3km}$ is the pooled average DIC increase at Sites 1267 and 607 in µmol/kg (42±15 µmol/kg for glacials and 30±16 µmol/kg for interglacials), $m_{Atlantic>3km}$ is the mass of water in the Atlantic Ocean below 3 km depth ($1.01*10^{20}$ kg), 12.011 is the mass of carbon (g/mol), and factor 10^{21} converts units from µg C to Gt C[76]. This calculation assumes that the magnitude of DIC increase reconstructed from Sites 1267 and 607 characterises the entire Atlantic Ocean below 3 km.

Significance Testing. Statistical comparisons of mean glacial/interglacial ε_{Nd} and reconstructed DIC before and after 950 ka was performed using one-tailed, two-sample *t*-test with unequal variance (Welch's *t*-test) in MATLAB (function ttest2). Significance was evaluated with α=0.05. Mean values and *p*-values for statistical tests are given in Supplementary Table 1.

Influence of alkalinity on pCO_2. Records of deep ocean sedimentary $CaCO_3$ content suggest pronounced changes in $CaCO_3$ sedimentation at the MPT. Expanded AABW resulting from reduced MOC lowered $CaCO_3$ preservation throughout the deep Atlantic at the MPT, as evidenced by carbonate %[25], sediment lightness (L*) and magnetic susceptibility records[50] (Supplementary Fig. 5). However, Site 1267 and 607 $\Delta[CO_3^{2-}]$ reconstructions do not show clear evidence for a transient $\Delta[CO_3^{2-}]$ rise across the MOC reduction (Fig. 2), as might be expected to occur within 5-10 kyr from "classic" carbonate compensation[39]. Site 1267 has an average sampling resolution of 9.2 kyr between 1,000 and 875 ka, and it is possible that this record lacks sufficient resolution to reconstruct a rapid carbonate compensation event. Site 607 has an average resolution of ~3 kyr, yet also does not show transient $\Delta[CO_3^{2-}]$ rises[25].

One possibility is that any $\Delta[CO_3^{2-}]$ rise from carbonate compensation is masked within these records; i.e., $\Delta[CO_3^{2-}]$ decreases less than expected from DIC increase alone due to the counteracting influence of increased TA from regional carbonate dissolution. In this scenario, ΔDIC derived from B/Ca would systematically underestimate true ΔDIC. To quantify this underestimation, Equation 3 shows that a 1 µmol/kg increase in TA from $CaCO_3$ dissolution increases $\Delta[CO_3^{2-}]$ by 0.27 µmol/kg. Estimates of the TA contribution from $CaCO_3$ dissolution in the modern ocean (termed TA^*, ref. 77) show TA^* of 0-10 µmol/kg for NADW and 20-30 µmol/kg for AABW. Assuming that the MOC shift at Site 1267 was associated with a 30 µmol/kg TA increase from enhanced $CaCO_3$ dissolution, $\Delta[CO_3^{2-}]$ would increase by 8.1 µmol/kg. This increase equates to ΔDIC of -13 µmol/kg, giving a revised post-950 ka glacial ΔDIC estimate of 63±16 µmol/kg from $\Delta[CO_3^{2-}]$ from Sites 1267 and 607, which is indistinguishable from the $\Delta[PO_4^{3-}]$-derived ΔDIC estimate of 49±24 µmol/kg.

Based on Site 607 $\Delta[CO_3^{2-}]$, Sosdian et al.[25] present a new model of carbonate compensation driven by changes in regional carbonate burial, and not local dissolution. In this model, the relationship between deep Atlantic TA and global ocean TA depends on Pacific $CaCO_3$ burial, giving a more complex relationship between deep Atlantic TA and potential CO_2 drawdown. Regardless, while the precise magnitude of ΔDIC may be sensitive to TA change from carbonate compensation and compensation mechanisms, the

conclusion of increased DIC in the deep Atlantic coeval with reduced MOC is not contingent on assuming constant TA.

Mixing between NADW and AABW. Supplementary Figure 3 shows relationships between Site 1267 [PO_4^{3-}], [CO_3^{2-}], $\delta^{13}C$[22], and relative NADW/AABW contributions from ε_{Nd}. Mixing curves are calculated using modern day endmember values for NADW and AABW defined from hydrographic data for ε_{Nd}, [PO_4^{3-}] and [CO_3^{2-}], and using late Holocene benthic foraminifer $\delta^{13}C$ for $\delta^{13}C_{DIC}$. Foraminifera were chosen to define the $\delta^{13}C_{DIC}$ endmembers considering the impact of anthropogenic carbon on hydrographic $\delta^{13}C_{DIC}$ (the 'Suess effect'), particularly in NADW[78]. Endmember values for ε_{Nd} and [Nd]: NADW = -14.0±0.5 ε units and [Nd] = 23.6 pmol/kg, AABW = -8.0±0.5 ε units and [Nd] = 26.1 pmol/kg (Y. Wu, pers. comm.); [PO_4^{3-}]: NADW = 1.1±0.05 µmol/kg, AABW = 2.25±0.01 µmol/kg[74]; [CO_3^{2-}]: NADW = 120±10 µmol/kg, AABW = 85±5 µmol/kg[74]; $\delta^{13}C$: NADW = 1.36±0.08‰ (0-5 ka from BOFS 11K, ref. 64); AABW = 0.27±0.1‰ (coretop from TN057-21; ref. 79). Mixing curves are calculated from simple two-component concentration and isotope mixture equations (example below for ε_{Nd}):

$$\varepsilon_{Nd\_mixture} = \frac{f_{NADW} * [Nd]_{NADW} * \varepsilon_{Nd\_NADW} + f_{AABW} * [Nd]_{AABW} * \varepsilon_{Nd\_AABW}}{f_{NADW} * [Nd]_{NADW} + f_{AABW} * [Nd]_{AABW}} \quad (8)$$

Preformed nutrients in AABW. In NADW and AABW endmembers, [PO_4^{3-}] is composed of preformed PO_4^{3-} and regenerated PO_4^{3-} components[80,81]:

$$[PO_4^{3-}]_{total}(\mu mol/kg) = [PO_4^{3-}]_{preformed} + [PO_4^{3-}]_{regenerated} \quad (9)$$

Following ref. 82, we use [PO_4^{3-}]$_{preformed}$ of 0.8 µmol/kg for NADW and 1.5 µmol/kg for AABW. These values agree with [PO_4^{3-}]$_{preformed}$ calculated from GEOTRACES[74] apparent oxygen utilisation (AOU) data ([PO_4^{3-}]$_{preformed}$ of 0.78±0.03 and 1.57±0.03 µmol/kg for NADW and AABW, respectively, using AOU of 55±5 and 115±5 µmol/kg for NADW and AABW, respectively, and an O_2:PO_4^{3-} ratio of 170 from ref. 26; calculation in ref. 82).

Additional curves in Supplementary Figure 3 show mixing between modern NADW and AABW with [PO_4^{3-}]$_{preformed}$ reduced by 25% and 50%, giving AABW [PO_4^{3-}

654 $]_{preformed}$ of 1.13 and 0.9 µmol/kg, respectively. Note that $[PO_4^{3-}]_{total}$ is kept constant, any
655 $[PO_4^{3-}]_{preformed}$ decrease is added to $[PO_4^{3-}]_{regenerated}$[81]. The addition of $[PO_4^{3-}]_{regenerated}$ adds
656 regenerated DIC, increasing DIC (117:1 ratio[26]), and thus decreasing $[CO_3^{2-}]$. The effect
657 of DIC addition on $[CO_3^{2-}]$ is calculated using Equation 3 (above). The effect on $\delta^{13}C$ is
658 calculated by assuming the added DIC possesses a constant $\delta^{13}C$ of -25‰ corresponding
659 to organic matter. Two-component mixing curves are then recalculated using the modern-
660 day NADW endmember values and the updated AABW endmember $[CO_3^{2-}]$ and $\delta^{13}C$
661 values.

662 Cross-plots of $[PO_4^{3-}]$, $[CO_3^{2-}]$ and $\delta^{13}C$ with ε_{Nd} show that reconstructed $[PO_4^{3-}]$
663 corresponds to mixing between modern NADW and AABW endmembers, while $[CO_3^{2-}]$
664 and benthic $\delta^{13}C$ imply mixing with AABW possessing lower $[CO_3^{2-}]$ and $\delta^{13}C_{DIC}$ than
665 modern (Supplementary Fig. 3). These observations can be reconciled by a higher
666 regenerated to preformed PO_4^{3-} ratio in mid-Pleistocene AABW compared to today. A
667 shift from $[PO_4^{3-}]_{preformed}$ to $[PO_4^{3-}]_{regenerated}$ would not change total $[PO_4^{3-}]$[81], but would
668 decrease AABW $[CO_3^{2-}]$ and $\delta^{13}C$ through excess regenerated ^{13}C-depleted organic
669 matter and sluggish air-sea gas exchange in the Southern Ocean. Mixing arrays calculated
670 with varying regenerated to preformed PO_4^{3-} ratios suggest that AABW in the Angola
671 Basin may have had up to 50% lower $[PO_4^{3-}]_{preformed}$ during the MPT compared to today,
672 particularly in glacials after 950 ka (Supplementary Fig. 3). This level of decreased
673 AABW $[PO_4^{3-}]_{preformed}$ is similar to estimates for the Last Glacial Maximum (LGM)[81],
674 when AABW $\delta^{13}C$ and $\Delta[CO_3^{2-}]$ were lower than today[14,63], and is consistent with the
675 proposed coupling between Southern Ocean nutrient utilisation and expanded AABW
676 through Southern Ocean surface buoyancy forcing[38].

677 Because modern AABW has more preformed nutrients than NADW, assuming
678 that modern AABW expanded in the past would have ventilated a greater portion of the
679 deep Atlantic through the Southern Ocean, where the biological pump is less efficient. In
680 this scenario, reduced MOC would both increase deep Atlantic DIC and increase
681 pCO_2[29,80]. For the MPT, if expanded AABW possessed 50% lower $[PO_4^{3-}]_{preformed}$, the
682 effect of preformed nutrients on pCO_2 would be minor. This is because AABW would
683 replace NADW of similar $[PO_4^{3-}]_{preformed}$, implying that deep Atlantic $[PO_4^{3-}]_{preformed}$

684 stayed relatively constant. This is critical for pCO_2 because it implies that reduced MOC
685 was not associated with a less efficient biological pump, and further implies that reduced
686 MPT pCO_2 required coupling between MOC and CO_2 outgassing in the Southern Ocean
687 (Fig. 4).

688 **Data availability.** The datasets generated during the current study are available as
689 Supplementary Tables 2 through 5 in the Supplementary Data, and will be publicly
690 accessible via the National Centers for Environmental Information (NCEI) following
691 acceptance. A persistent web link to the dataset will be provided at that time.

692

693 **Methods References.**

694 51. Lisiecki, L.E., & Raymo, M.E. A Pliocene-Pleistocene stack of 57 globally
695 distributed benthic $\delta^{18}O$ records. *Paleoceanography* **20**, PA1003 (2005).

696 52. Yu, J. *et al.* Responses of the deep ocean carbonate system to carbon reorganization
697 during the Last Glacial-interglacial cycle. *Quat. Sci. Rev.* **76**, 39-52 (2013).

698 53. Rosenthal, Y., Boyle, E.A., & Labeyrie, L. Last glacial maximum paleochemistry and
699 deepwater circulation in the Southern Ocean: Evidence from foraminiferal
700 cadmium. *Paleoceanography* **12**, 787-796 (1997).

701 54. Barker, S., Greaves, M., & Elderfield, H. A study of cleaning procedures used for
702 foraminiferal Mg/Ca paleothermometry. *Geochem. Geophys. Geosyst.* **4**, 8407
703 (2003).

704 55. Yu, J., Elderfield, H., Greaves, M., & Day, J. Preferential dissolution of benthic
705 foraminiferal calcite during laboratory reductive cleaning. *Geochem. Geophys.*
706 *Geosyst.* **8**, Q06016 (2007).

56. Ford, H.L., Sosdian, S.M., Rosenthal, Y., & Raymo, M.E. Gradual and abrupt changes during the Mid-Pleistocene Transition. *Quat. Sci. Rev.* **148**, 222-233 (2016).

57. Yu, J., Day, J., Greaves, M., & Elderfield, H. Determination of multiple element/calcium ratios in foraminiferal calcite by quadrupole ICP-MS. *Geochem. Geophys. Geosyst.* **6**, Q08P01 (2005).

58. Roberts, N.L., Piotrowski, A.M., McManus, J.F., & Keigwin, L.D. Synchronous deglacial overturning and water mass source changes. *Science* **327**, 75-78 (2010).

59. Tanaka, T. *et al.* JNdi-1: a neodymium isotopic reference in consistency with LaJolla neodymium. *Chem. Geol.* **168**, 279-281 (2000).

60. Jacobsen, S.B. & Wasserburg, G.J. Sm-Nd isotopic evolution of chondrites. *Earth Planet. Sci. Lett.* **50**, 139-155 (1980).

61. Rae, J.W.B., Foster, G.L., Schmidt, D.N. & Elliott, T. Boron isotopes and B/Ca in benthic foraminifera: Proxies for the deep ocean carbonate system. *Earth Planet. Sci. Lett.* **302**, 403-413 (2011).

62. Raitzsch, M., Hathorne, E.C., Kuhnert, H., Groeneveld, J. & Bickert, T. Modern and late Pleistocene B/Ca ratios of the benthic foraminifer *Planulina wuellerstorfi* determined with laser ablation ICP-MS. *Geology* **39**, 1039-1042 (2011).

63. Yu, J. *et al.* Responses of the deep ocean carbonate system to carbon reorganization during the Last Glacial-interglacial cycle. *Quat. Sci. Rev.* **76**, 39-52 (2013).

64. Yu, J., Elderfield, H. & and Piotrowski, A. Seawater carbonate ion-δ^{13}C systematics and application to glacial-interglacial North Atlantic Ocean circulation. *Earth Planet. Sci. Lett.* **271**, 209-220 (2008).

65. van Heuven, S., Pierrot, D., Rae, J.W.B., Lewis, E., & Wallace, D.W.R. MATLAB Program Developed for CO2 System Calculations. ORNL/CDIAC-105b. Carbon Dioxide Information Analysis Center, Oak Ridge National Laboratory, U.S. Department of Energy, Oak Ridge, Tennessee (2011).

66. Yu, J. *et al*. Loss of Carbon from the Deep Sea since the Last Glacial Maximum. *Science* **330**, 1084-1087 (2010).

67. Sexton, P.F. & Barker, S. Onset of 'Pacific-style' deep-sea sedimentary carbonate cycles at the mid-Pleistocene transition. *Earth Planet. Sci. Lett.* **321-322**, 81-94 (2012).

68. Boyle, E.A. Cadmium: Chemical tracer of deepwater paleoceanography. *Paleoceanography* **3**, 471-489 (1988).

69. Marchitto, T.M. & Broecker, W.S. Deep water mass geometry in the glacial Atlantic Ocean: A review of constraints from the paleonutrient proxy Cd/Ca. *Geochem. Geophys. Geosyst.* **7**, Q12003 (2006).

70. de Baar, H.J.W., Saager, P.M., Nolting, R.F., & van der Meer, J. Cadmium versus phosphate in the world ocean. *Mar. Chem.* **46**, 261-281 (1994).

71. Elderfield, H., & Rickaby, R.E.M. Oceanic Cd/P ratio and nutrient utilisation in the glacial Southern Ocean. *Nature* **405**, 305-310 (2000).

748 72. Baars, O., Abouchami, W., Galer, S.J.G., Boye, M., & Croot, P.L. Dissolved
749 cadmium in the Southern Ocean: Distribution, speciation, and relation to
750 phosphate. *Limnol. Oceanogr.* **59**, 385-399 (2014).

751 73. Quay, P., & Wu, J. Impact of end-member mixing on depth distributions of $\delta^{13}C$,
752 cadmium and nutrients in the N. Atlantic Ocean. *Deep-Sea Res. II* **116**, 107-116
753 (2015).

754 74. Mawji, E. *et al.*, The GEOTRACES Intermediate Data Product 2014. *Mar. Chem.*
755 **177**, 1-8 (2015).

756 75. Roshan, S., & Wu, J. Cadmium regeneration within the North Atlantic. *Global*
757 *Biogeochem. Cycles* **29**, 2082-2094 (2015).

758 76. Clark, W.C. (ed.) *Carbon Dioxide Review: 1982*, p. 467, Oxford University Press,
759 New York (1982).

760 77. Feely, R.A., Sabine, C.L., Lee, K., Millero, F.J., Lamb, M.F., Greeley, D., Bullister,
761 J.L., Key, R.M., Peng, T.-H., Kozyr, A., Ono, T. & Wong, C.S. In situ calcium
762 carbonate dissolution in the Pacific Ocean. *Global Biogeochem. Cycles* **16**, 1144
763 (2002).

764 78. Olsen, A. & Ninnemann, U. Large $\delta^{13}C$ Gradients in the Preindustrial North Atlantic
765 Revealed. *Science* **330**, 658-659, doi:10.1126/science.1193769 (2010).

766 79. Ninnemann, U.S. & Charles, C.D. Changes in the mode of Southern Ocean
767 circulation over the last glacial cycle revealed by foraminiferal stable isotopic
768 variability. *Earth Planet. Sci. Lett.* **201**, 383-396 (2002).

769 80. Marinov, I., Gnanadesikan, A., Sarmiento, J.L., Toggweiler, J.R., Follows, M. &
770 Mignone, B.K. Impact of oceanic circulation on biological carbon storage in the
771 ocean and atmospheric pCO_2. *Global Biogeochem. Cycles* **22**, GB3007 (2008).

772 81. Jaccard, S.L., Galbraith, E.D., Sigman, D.M., Haug, G.H., Francois, R., Pedersen,
773 T.F., Dulski, P., & Thierstein, H.R. Subarctic Pacific evidence for a glacial
774 deepening of the oceanic respired carbon pool. *Earth Planet. Sci. Lett.* **277**, 156-
775 165 (2009).

776 82. Broecker, W.S., Takahashi, T., and Takahashi, T. Sources and Flow Patterns of Deep-
777 Ocean Waters as Deduced from Potential Temperature, Salinity, and Initial
778 Phosphate Concentration. *J. Geophys. Res.* **90**, 6925-6939 (1985).

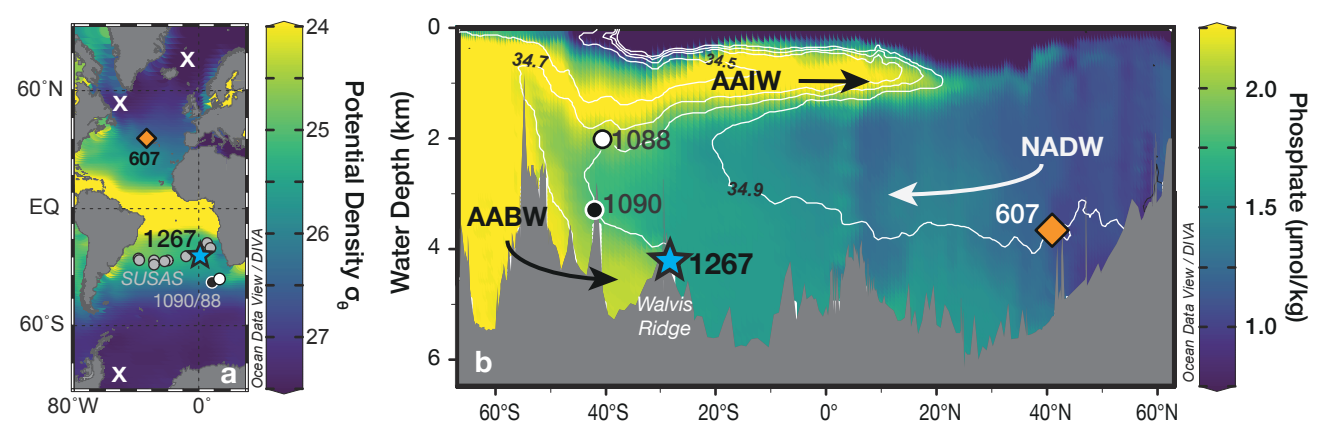
60°N
EQ
60°S
80°W
0°
607
1267
SUSAS
1090/88
a
Ocean Data View / DIVA
24
25
26
27
Potential Density σθ
Water Depth (km)
0
2
4
6
34.7
34.5
34.9
AAIW
NADW
AABW
1088
1090
607
1267
Walvis
Ridge
b
60°S
40°S
20°S
0°
20°N
40°N
60°N
Ocean Data View / DIVA
2.0
1.5
1.0
Phosphate (µmol/kg)

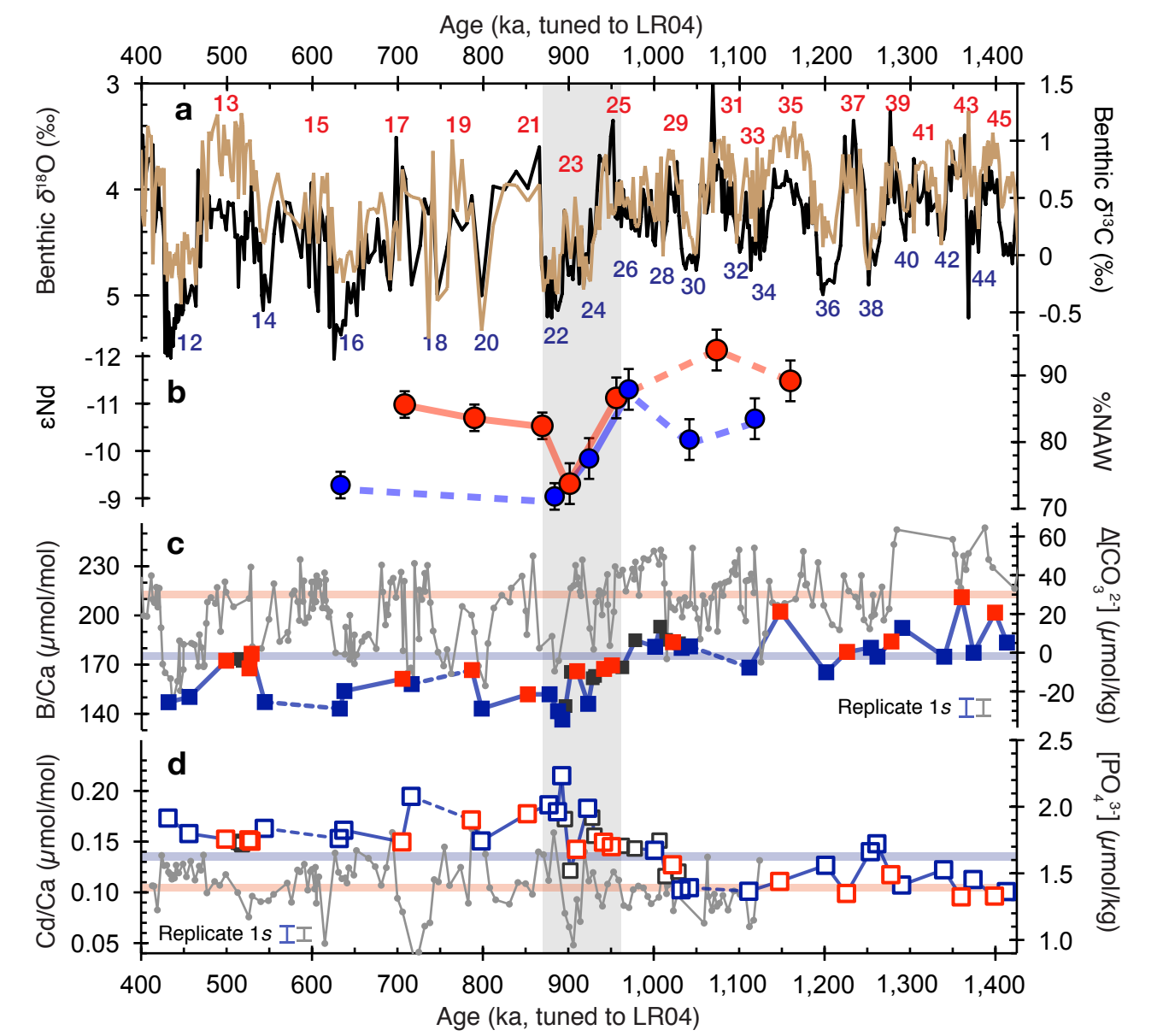
Age (ka, tuned to LR04)
400
500
600
700
800
900
1,000
1,100
1,200
1,300
1,400
a
Benthic δ18O (‰)
Benthic δ13C (‰)
3
4
5
1.5
1
0.5
0
-0.5
12
13
14
15
16
17
18
19
20
21
22
23
24
25
26
28
29
30
31
32
33
34
35
36
37
38
39
40
41
42
43
44
45
b
εNd
%NAW
-12
-11
-10
-9
90
80
70
c
B/Ca (μmol/mol)
Δ[CO3 2-] (μmol/kg)
230
200
170
140
60
40
20
0
-20
Replicate 1s
d
Cd/Ca (μmol/mol)
[PO4 3-] (μmol/kg)
0.20
0.15
0.10
0.05
2.5
2.0
1.5
1.0
Replicate 1s
Age (ka, tuned to LR04)

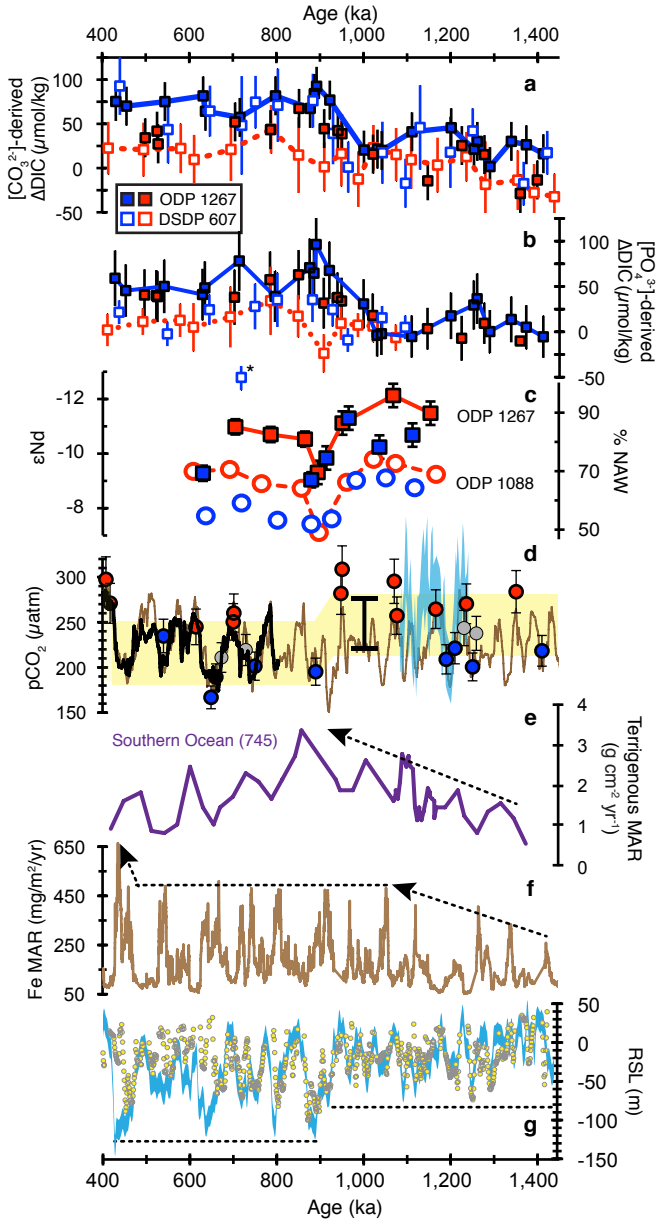
Age (ka)
400
600
800
1,000
1,200
1,400
a
[CO3 2-]-derived ΔDIC (μmol/kg)
100
50
0
-50
ODP 1267
DSDP 607
b
[PO4 3-]-derived ΔDIC (μmol/kg)
100
50
0
-50
c
εNd
-12
-10
-8
ODP 1267
ODP 1088
% NAW
90
70
50
d
pCO2 (μatm)
300
250
200
150
e
Southern Ocean (745)
Terrigenous MAR (g cm-2 yr-1)
4
3
2
1
0
f
Fe MAR (mg/m2/yr)
650
450
250
50
g
RSL (m)
50
0
-50
-100
-150
400
600
800
1,000
1,200
1,400
Age (ka)

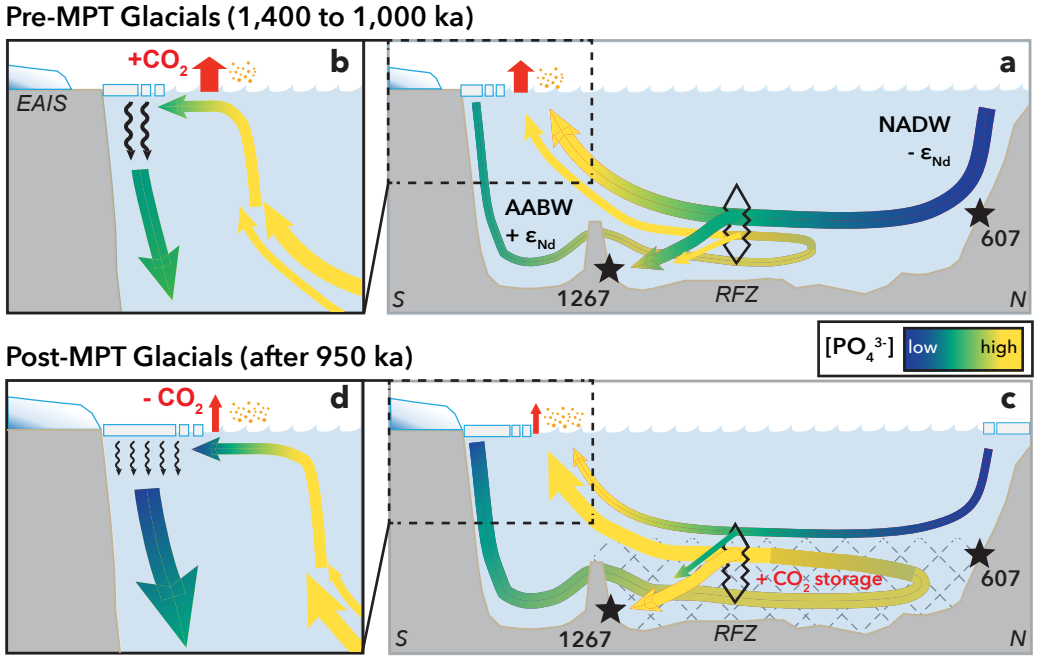
Pre-MPT Glacials (1,400 to 1,000 ka)
+CO2
b
EAIS
a
NADW
- εNd
AABW
+ εNd
607
1267
RFZ
S
N
[PO4 3-]
low
high
Post-MPT Glacials (after 950 ka)
- CO2
d
c
+ CO2 storage
607
1267
RFZ
S
N